Du et al. *Microsystems & Nanoengineering* (2026)12:106
https://doi.org/10.1038/s41378-026-01222-3

Microsystems & Nanoengineering
www.nature.com/micronano

ARTICLE Open Access

Extreme sensitivity label-free biosensing platform based on topologically disruptive phase nano-optics

Fusheng Du[1], Manon Gireau[2], Joelle Youssef[3,4], Georges Humbert[3], Sébastien Vergnole[4], Frédéric Dumas-Bouchiat[2]✉, Corinne Champeaux[2]✉ and Shuwen Zeng[1,5]✉

Abstract

Label-free plasmonic biosensors hold significant promise for advancing molecular biology research and enabling early disease diagnostics, particularly in detecting trace amounts of target molecules in highly diluted solutions. However, conventional plasmonic biosensors face substantial challenges in detecting lower-molecule-weight (<500 Da) biomolecules, especially at extreme low concentrations. To overcome this limitation, a novel plasmonic biosensor platform based on enhanced topological phase singularity has been proposed. Herein, we demonstrate that extremely small-sized (<3 nm) silver nanoparticles, embedded in aluminum oxide with a highly ordered configuration and sub-nanometer alignment and inter-particle spacing (<1 nm), and covered by a gold film, exhibit a topologically dark reflection and produces a sharp phase change, which ultimately presents as a significant shift in the reflected beam's position. By precisely modulating the concentration of silver nanoparticles, a largest position shift of 554.3 μm was achieved in calibration experiments with an extreme sensitivity of 3.27×10^8 nm RIU^{-1} (refractive index unit). The refractive index resolution was determined to be 3.67×10^{-7} RIU with a 0.12 μm position resolution. We also demonstrated the ability of the proposed biosensor platform to detect extremely low-molecular-weight (244 Da) biotin biomolecules at femtomolar concentrations. Furthermore, in target biosensing experiments, the plasmonic biosensor platform successfully directly detected small cytokine biomarker (TNF-α) in real-time at 100 zeptomolar (10^{-21} mol L^{-1}), highlighting its potential for extreme-sensitive biosensing applications.

Introduction

Label-free optical biosensing has become an increasingly important tool in modern bioanalytics[1–3]. Unlike traditional detection methods that require fluorescent dyes[4] or enzymatic tags[5], label-free optical sensors allow the real-time, non-invasive monitoring of biomolecular interactions directly in their native environments[6]. For example, photonic-crystal fiber architectures have recently pushed label-free sensing to the attomolar regime[7]. Hybrid plasmonic-microfluidic platforms have enabled to discriminate different forms of Alzheimer's disease protein ($A\beta_{42}$) at range of ~30–170 pg/mL[8]. Meanwhile, the label-free biosensors based on dual lossy-mode resonance have allowed the simultaneous quantification of inflammation-related biomarkers (C-reactive protein and D-dimer) with below 1 μg/mL[9]. Thus, these sensors can be applied not only for pharmaceutical development but also in other useful applications including clinical diagnostics[10,11] and environmental analysis[12,13], without changing the natural behavior of molecules.

Conventional plasmonic biosensors, typically based on surface plasmon polaritons (SPPs)[14] or localized surface plasmons (LSPs)[15], detect target molecules by tracking the

Correspondence: Frédéric Dumas-Bouchiat (frederic.dumas-bouchiat@unilim.fr) or Corinne Champeaux (corinne.champeaux@unilim.fr) or Shuwen Zeng (shuwen.zeng@cnrs.fr)
[1]Light, Nanomaterials & Nanotechnologies (L2n), CNRS-UMR 7076, University of Technology of Troyes, 10004 Troyes, France
[2]Institute of Research for Ceramics (IRCER), CNRS-UMR 7315, University of Limoges, 87000 Limoges, France
Full list of author information is available at the end of the article
These authors contributed equally: Fusheng Du, Manon Gireau

shift in the resonance condition of light. This resonance shift, often measured via angle or wavelength interrogation, is sensitive to the refractive index changes that occur when biomolecules bind to a metal surface[16–18]. However, these plasmonic sensors are not capable to achieve the detection at levels down to femtograms or even attograms per milliliter.

Unlike the above-mentioned approaches, phase-sensitive techniques utilize the optical phase signal change induced by the biological interactions at the sensing surface[19–23]. The challenges of all phase-sensitive plasmonic detection are to reach the "phase singularities" under the resonance conditions, also known as optical dark points, where the reflected light intensity drops to quasi-zero while the phase response will undergo an ultra-sharp and nonlinear variation[24]. These singularities give rise to dramatic enhancements in detection sensitivity.

In this work, for the first time, the precise control of nanoparticle arrays less than 3 nm in diameter have been employed for achieving the extreme singularity for the optical phase jump for plasmonic biosensors. These nanoparticles are positioned with a highly ordered configuration. Our system consists of ultra-small silver nanoparticles embedded within a thin aluminum oxide dielectric matrix topped with a gold film, made through a dual pulsed laser source[25,26]. This nanocomposite ensures an efficient interparticle coupling distances, fostering strong near-field coupling and the emergence of coherent collective plasmonic modes. As a result, the platform supports nanoscale optical cavities that exhibit sharp, controllable phase singularities.

The unique property of this system is that small changes in local refractive index near a singularity induce large lateral displacements in the reflected light beam—a phase transduction effect that serves as the basis for biosensing. By tuning the volumetric concentration of silver nanoparticles (2–16%), we achieve precise control over both the spectral location and sharpness of the singularity. Experimental calibration using standard refractive index media demonstrates beam displacements up to 554.3 μm, corresponding to a phase singularity-induced beam-displacement sensitivity of 3.27×10^8 nm/RIU. The system achieves a refractive index resolution of 3.67×10^{-7} RIU and spatial resolution down to 0.12 μm, representing a significant enhancement over conventional SPR and LSPR platforms. Crucially, our label-free sensor is capable of detecting extremely small biomolecules—such as biotin (244 Da) at femtomolar concentrations—and small cytokine molecules like tumor necrosis factor-alpha (TNF-α), an important cancer biomarker at 100 zeptomolar (10^{-21} M) levels. These features make our platform highly sensitive, robust, and versatile, offering a new direction in optical biosensing technology suitable for detecting a broad range of biological and chemical targets with unprecedented sensitivity.

Results

Fabrication and characterization of the plasmonic sensing substrate

The fabricated plasmonic sensing substrate is shown in the Fig. 1a, b, which comprises 3 layers silver nanoparticles (Ag NPs) uniformly embedded in aluminum oxide (Al_2O_3), and thin films of gold (Au). Silver is chosen for its outstanding and well-established, plasmonic performances in the visible range, driven by its highly negative real permittivity and low optical losses. Embedding 2.3 nm diameter Ag NPs within a dense 12 nm Al_2O_3 matrix preserves their stability while significantly enhancing their plasmonic response, as discussed in the following together with FDTD simulations. This configuration facilitates near-field coupling between localized surface plasmons in Ag NPs and propagating surface plasmons at the 48 nm thick Au sensing interface.

The experimental surface plasmon resonance (SPR) reflectance spectra in deionized water of plasmonic sensing substrates with varying concentrations of Ag NPs (2%, 8% and 16%) are shown in Fig. 1c. A dramatic reduction in reflectivity occurred when the concentration of Ag NPs is at 16%, with the minimum reflectance reaching approximately 0.02. This value represents an order-of-magnitude decrease compared to the pure Au film substrate (0.13), demonstrating the enhanced optical absorption achieved through the Ag NPs incorporation. The substantial reflectance suppression at 16% Ag NPs concentration suggests strong potential for generating phase singularities, making this composition particularly promising for advanced plasmonic applications.

However, the substrates with lower Ag NPs concentrations (2% and 8%) showed minimal differences in minimum reflectance compared to the pure Au film (Fig. 1d). To better understand how the minimum reflectivity varies with Ag NPs concentration, theoretical calculations based on the Maxwell Garnett effective medium equations[27] are performed:

$$n = \sqrt{n_{Al_2O_3}^2 * \frac{(2 * A + B)}{(-A + B)}} \tag{1}$$

$$A = f * \left(n_{Ag}^2 - n_{Al_2O_3}^2\right) \tag{2}$$

$$B = n_{Ag}^2 + 2 * n_{Al_2O_3}^2 \tag{3}$$

Where n_{Ag} is the refractive index of silver, $n_{Al_2O_3}$ is the refractive index of Al_2O_3 matrix, and f is the concentration of the Ag NPs. As evident from Fig. 1e, f, the

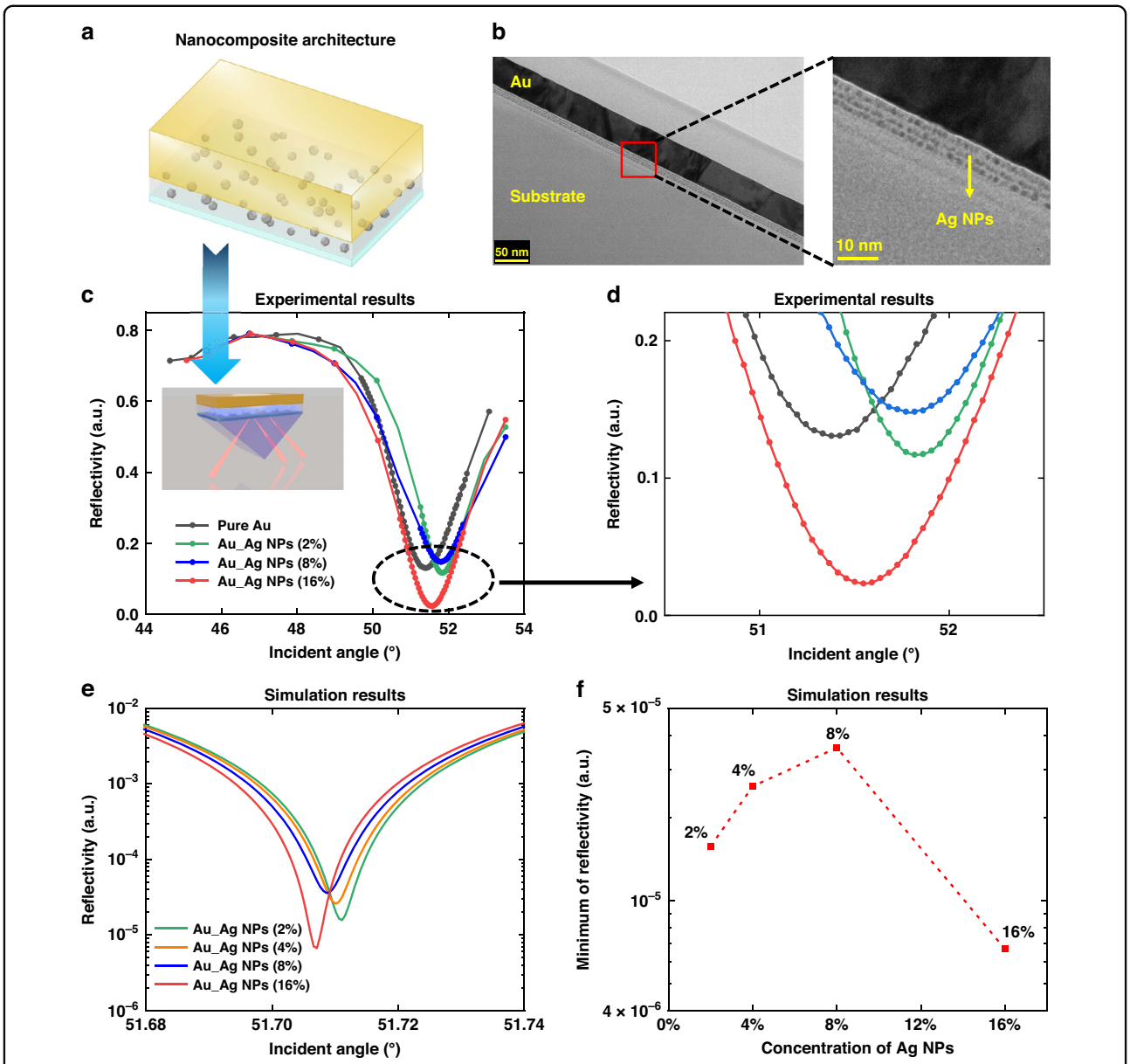

Fig. 1 Structural design and optical characterization of the plasmonic sensing substrate. a Schematic illustration of multilayer substrate architecture. **b** Cross-sectional HRTEM image of the fabricated sensing substrate. **c** Experimental reflectance curve of different sensing substrates (Au_Ag NPs (2%, 8% and 16%)) and a control sample with pure Au. **d** Detailed view of the dashed region from (**c**). **e** Simulation reflectivity curve of Au_Ag NPs with varying Ag NPs concentrations. **f** Minimum reflectivity as a function of Ag NPs concentrations with an optimal minimum at 16%

minimum reflectivity of the SPR initially exhibits a slight increase with higher Ag NPs concentration. However, at 16% Ag NPs, the reflectivity drops sharply to its lowest value, aligning well with our experimental observations. Furthermore, an extended analysis was performed by quantifying the minimum reflectance for a larger range of 1–25% Ag NPs concentrations, as confirmed in the Fig. S1. The resulting trend reveals that excessively high concentrations of Ag NPs, such as 25%, do not yield further reductions in SPR reflectivity. In addition, Fig. S1 shows that 18% Ag NPs and 16% NPs exhibit similar minimum reflectance values. However, the full width at half maximum (FWHM) of the 18% Ag NPs is broader than that of the 16% Ag NPs. Consequently, the 16% Ag NPs demonstrates higher sensing resolutions for molecular detections.

The nanocomposite architectures are fabricated using Pulsed Laser Deposition associated with a Free Cluster Generator, which allows precise control of both propagative and localized surface plasmon resonance effects. To

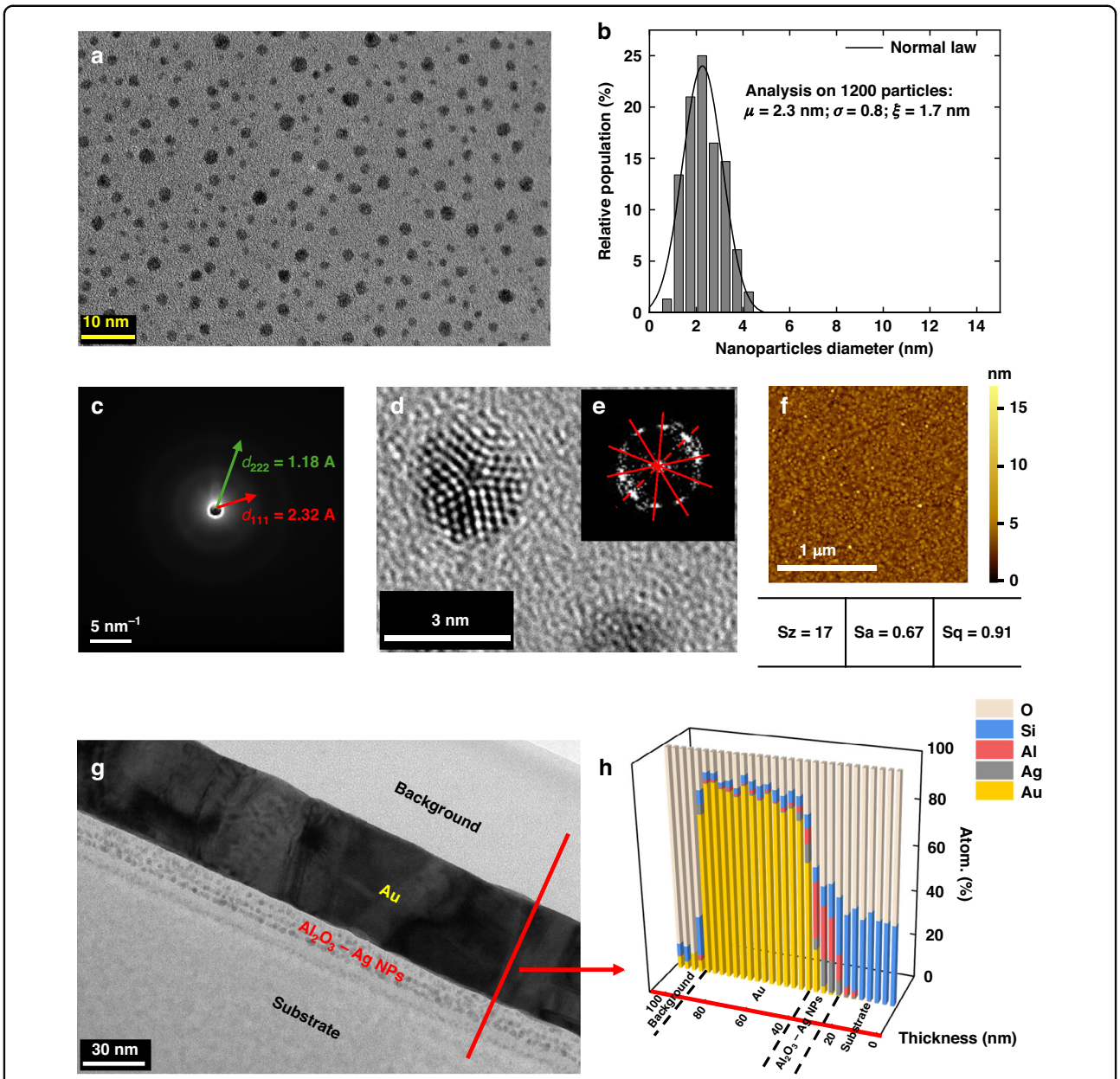

Fig. 2 Characterization of the nanocomposite architectures. a HR-TEM image of silver nanoparticles deposited on a TEM grid, 200000× magnification. **b** The corresponding statistical analysis over the diameter of the particles. The center of the distribution and mean diameter is μ = 2.3 nm, the standard deviation is σ = 0.8 and the Full Width at Half Maximum (FWHM) is ξ = 1.7 nm. **c** Selected Area Electron Diffraction (SAED) pattern of the silver nanoparticles with d_{111} = 2.32 Å and d_{222} = 1.18 Å. **d** Zoom on a single crystallized silver nanoparticle whose diameter is 2.5 nm, 600000× magnification. **e** Corresponding Fast Fourier Transform (FFT) of the single silver particle, highlighting its five-fold symmetry. **f** Atomic Force Microscope (AFM) image of a 48 nm-thick gold layer. The S_z corresponds to the peak to peak; the S_a is the image-average roughness and the S_q represents the root mean square (RMS) roughness. **g** HR-TEM cross section image presents the architecture of the nanocomposite, 100000× magnification. **h** The corresponding EDS profile line analysis pointing out the atomic percentages of oxygen, aluminum, silicon, silver and gold against sample height

ensure tight control over the architecture of the final sensing platform, each constituent (nanoparticles and thin films) was synthesized individually and characterized independently, allowing the optimal deposition conditions to be precisely defined beforehand.

As shown in Fig. 2a, b. Ag NPs are analyzed using Transmission Electron Microscopy (TEM JEOL 2100 F) in high-resolution mode (HR-TEM) to characterize their size, distribution, and shape. The nanoparticles are deposited onto copper grids covered with a carbon

membrane, placed on the rotated substrate holder inside the main chamber. Figure 2a shows randomly arranged Ag NPs on the amorphous carbon membrane. A surface coverage of approximately 12% was achieved after a 15 min deposition under the conditions described in Table S1. A statistical analysis (Fig. 2b) performed on the HR-TEM images using ImageJ software, based on the distribution in size of a sample containing 1200 particles, revealed a mean particle diameter of 2.3 nm with a standard deviation of 0.8 nm, and a full width at half maximum (FWHM) of 1.7 nm. The shape factor ($F = \sqrt{\frac{4\pi A}{P^2}}$, where A is the area and P is the perimeter of the particle), which quantifies the degree of circularity (with 1 indicating a perfect circle), was found to be approximately 0.8, suggesting that the nanoparticles exhibit a nearly spherical shape in three dimensions. Selected Area Electron Diffraction (SAED) pattern (Fig. 2c) shows two concentric rings which confirms the crystalline nature of the randomly distributed particles. The measured interplanar spacings, $d_{hkl} = 2.32$ Å and 1.18 Å, correspond to the (111) and (222) planes, respectively, of face-centered cubic (FCC) silver nanoparticles, in agreement with the JCPS 00-004-0783 card.

A zoom-image of a single particle with a diameter of 2.5 nm presented in Fig. 2d exhibits a decahedral shape along the [001] direction, consistent with previous reports by Flores et al.[28]. The Fast Fourier Transform (FFT) of the image in Fig. 2e confirms the five-fold symmetry of the particle, supporting the decahedral structure, which is a characteristic feature of in-flight synthesized particles. These TEM analyses are crucial as the properties of nanoparticles are highly related to both their size and shape. The quasi-monodisperse size distribution produced by the nanoparticle generator ensures a high level of control over the properties of the nanoparticles, making it a valuable approach for tailoring particle's characteristics.

Al_2O_3 thin films were deposited on glass substrates to investigate the characteristics of the matrix, before silver nanoparticles addition. X-ray Photoelectron Spectroscopy was carried out by a Kratos Axis Ultra DLD spectrometer, equipped with a monochromate Al Kα source (12 mA, 15 kV) (Fig. S2). Oxygen/aluminum ratio was found to be 1.4, closely matching the stoichiometry of the target, demonstrating the congruent transfer capabilities of the PLD setup. X-ray diffraction diagram obtained in θ-2θ configuration using a Bruker D8 Advanced A25, of Al_2O_3 thin films exhibits an amorphous structure (Fig. S3). The UV-visible spectrum exhibits an absorption peak at 432 nm, attributed to the localized surface plasmon resonance (LSPR) of Ag NPs embedded within the Al_2O_3 matrix (Fig. S4). This resonance wavelength, well described by the classical Mie theory for Ag NPs, confirms the metallic behavior of Ag NPs and the quality of the interface NPs - oxide matrix, without oxidation at the surface of the NPs.

The thickness and roughness of gold thin films on the top of the architecture are measured by Atomic Force Microscopy (Bruker dimension ICON) in tapping mode. The film exhibits a thickness of 48 ± 2 nm and an average RMS roughness below 1 nm (Fig. 2f). The 17 nm peak to peak value is attributed to the underlying glass substrate. XRD revealed characteristic peaks of polycrystalline gold crystallized in the FCC system, preferentially orientated along the [111] direction (Fig. S5). The conductivity of gold thin films measured with a co-linear four-point probe method of 2.5×10^7 S.m^{-1} is closely matching the bulk gold conductivity of 4.6×10^7 S.m^{-1}, highlighting the metallic behavior and high quality of the thin film.

A cross-section of the entire biosensor architecture, consisting of an Au film deposited on Ag NPs doped Al_2O_3 nanocomposite thin film covering a glass substrate, was prepared using a Focused Ion Beam (ZEISS Crossbeam 550) and observed by high resolution TEM microscopy. Figure 2g clearly shows, on the amorphous glass substrate, the dense and amorphous Al_2O_3 matrix with embedded Ag NPs. The measured thickness of this composite layer is around 12 nm, as expected. The rows of atoms inside the particles are visible, consistent with the crystallized structure previously observed. Ag NPs exhibit smooth, well-defined, and contamination-free interfaces with their surrounding matrix, which is essential to support LSPR effects. The continuous gold layer is finishing the architecture. The rows of atoms and several grains with different orientations can be seen, consistent with the polycrystallinity deduced from XRD. As expected, the measured thickness is around 48 nm. The smooth surface can effectively minimize scattering of surface plasmons[29].

Figure 2h presents the energy dispersive X-ray spectroscopy (EDS) line profile analysis of the nanocomposite shown in Fig. 2g. This analysis supports the expected elementary composition described above, with silicon and oxygen in the glass substrate, aluminum, oxygen and silver in the thin nanocomposite layer, and finally gold. This analysis validates the measured thicknesses for both the nanocomposite and gold layer and supports the absence of interdiffusion provided by the ambient temperature deposition. The embedded silver nanoparticles in the Al_2O_3 matrix covered by the gold layer represent a biocompatible structure with a straightforward biofunctionalization. No signs of porosity are observed between layers and contamination-free interfaces are ensured by the single reactor deposition technique developed. This process, illustrated in Fig. 3 and Fig. S6 (see Materials and Methods for details), provides a flexible and well-controlled approach for designing a wide range of complex nano-scaled structures.

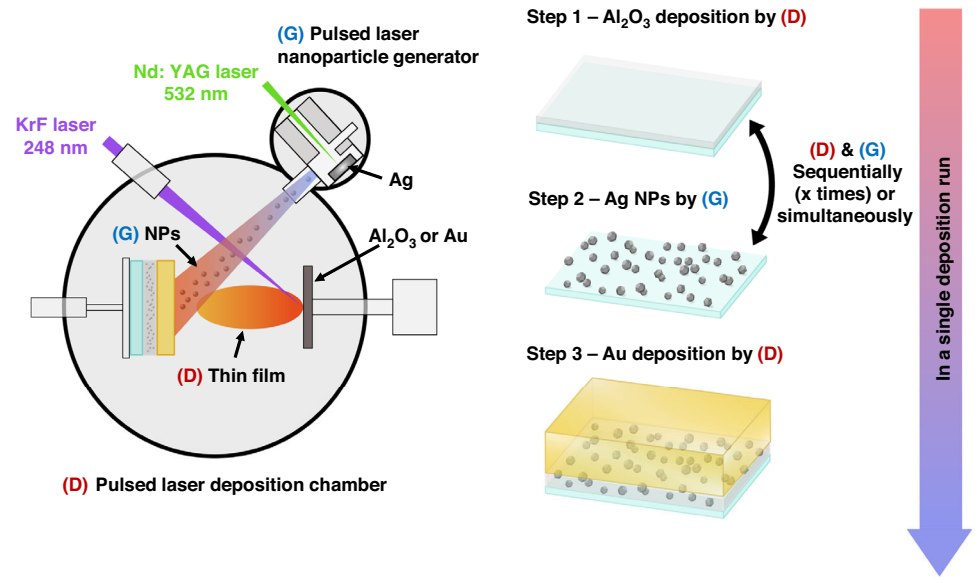

Fig. 3 Schematic representation of the nanocomposite sensors synthesis. The nanostructure is fabricated inside the reactor within a single deposition run. Thin films are grown by Pulsed Laser Deposition (PLD), while the silver nanoparticles are synthesized using a dedicated nanoparticles generator. The aluminium oxide matrix and silver nanoparticles are deposited by combining the PLD (D) and the nanoparticles generator (G), either sequentially (x times) or simultaneously. In the final step, a gold top-layer is deposited by PLD

Goos-Hänchen shift-based sensing mechanism

In this work, we employed a novel refractive index sensing approach based on lateral position shift, offering an alternative to conventional SPR interrogation methods that rely on angular or wavelength variations. The lateral position shift, known as the Goos-Hänchen (GH) shift, occurs when a linearly polarized incident beam undergoes total internal reflection at an interface[30–32]. This phenomenon arises due to the spatial displacement of the reflected beam, which is related to the phase change of the reflected light[33]. The magnitude of the GH shift is determined by differentiating the reflection phase change with respect to the incident angle. On a plasmonic substrate, this shift can be significantly enhanced due to the sharp phase transition occurring at the resonance angle. As illustrated in Fig. 4a, the spatial separation between reflected P- and S-polarized light arises due to their phase difference after reflection. According to the stationary phase theory, the GH shift in Kretschmann structure is defined as following equation[34]:

$$\Delta GH = -\frac{\lambda}{2\pi \cdot n_1}\frac{\Delta\phi_p - \Delta\phi_s}{\Delta\theta} \quad (4)$$

where λ is the wavelength of incident light, n_1 is the refractive index of the prism, ϕ is the optical phase of reflected light and θ is incident angle.

The custom-built optical system designed to measure the differential GH shift is shown in Fig. 4b. To evaluate the sensing performance across the visible to near-

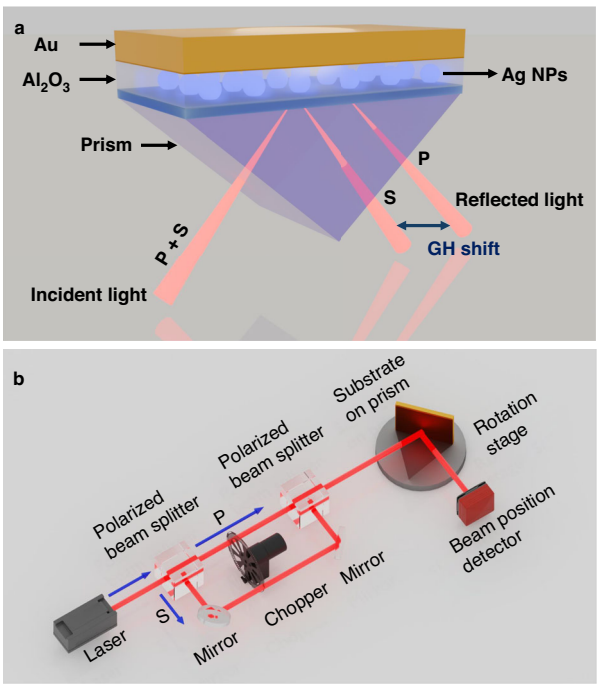

Fig. 4 Concept and optical setup of the GH Shift-based plasmonic biosensor. a Schematic illustration of the plasmonic biosensor utilizing a hybrid Ag NPs-Au sensing substrate. The incident beam, consisting of both P- and S-polarized components, is coupled to the substrate via a prism to facilitate the excitation of surface plasmons. **b** Experiment setup for measuring the GH shift from the nanocomposite substrate. A laser source with wavelengths of 785 nm and 633 nm is employed for excitation

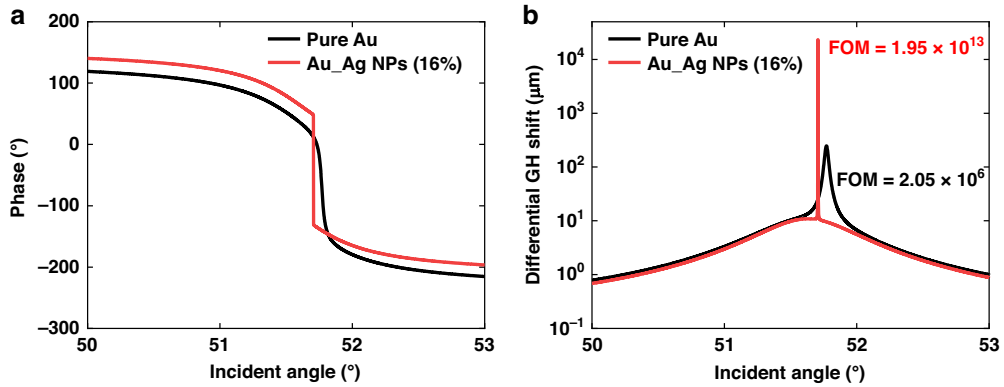

Fig. 5 Enhancement of the differential GH shift induced by phase singularity. a The calculated phase change of Au_Ag NPs (16%) in comparison with pure Au substrate at 785 nm. **b** Comparison of differential GH shift between Au_Ag NPs (16%) and pure Au substrates

infrared (NIR) region, a 633 nm He-Ne laser (HNL100LB, Thorlabs) and a 785 nm diode laser (ROUSB-785-PLR-80, Coherent Inc.) were employed. The incident beam was divided into P- polarized and S-polarized components using a polarizing beam splitter (PBS, PBS202, Thorlabs) and later recombined. A mechanical chopper (SRS542, Stanford Research Systems) placed between the PBS pair was used to periodically alternate the light polarization, facilitating continuous comparison of the lateral beam positions. This capability is essential for real-time detection of refractive index changes. To enhance the differential GH shift and ensure maximum sensitivity, the sensing substrate mounted on an SF11 prism was aligned at the resonance angle using a rotation stage. The reflected beams of P- and S-polarized light were acquired each 0.05 s using a position-sensitive detector (PDP90A, Thorlabs Inc., France), with a position resolution of 0.05 μm. As shown in the Fig. S7, the experimentally measured noise after applying a 5 s smoothing filter to the real-time raw signal is 0.12 μm, which represents the effective system noise level under detecting conditions, including chemical noise, temperature drift, and inter-cycle variability.

As illustrated in Fig. 5a, b, the phase singularity becomes visually apparent through phase differentiation, manifested as a GH shift (Eq. 4). Under 785 nm excitation, the Au_Ag NPs (16%) substrate exhibits an exceptionally large differential GH shift peak due to the singular phase jump. This peak reaches 23,369.2 μm, which is more than two orders of magnitude greater than that of the pure Au substrate. Moreover, the GH shift peak on the Au_Ag NPs (16%) substrate demonstrates an extremely narrow FWHM of 0.001°, which is over 100-fold sharper than the 0.105° observed for pure Au. Notably, the achieved maximum GH shift surpasses current cutting-edge GH shift sensing substrates, even those with intricate nanostructures[35,36], by an order of magnitude in both magnitude and spectral sharpness.

The figure of merit (FOM) of this plasmonic sensor was also calculated for GH shift as shown in Fig. 5b. FOM is defined as $(\Delta GH/\Delta n)/FWHM$, where ΔGH signifies the changes in differential GH shift, and Δn represents the changes in the medium refractive index. The FOMs marked in the Fig. 5b are calculated at $\Delta n = 10^{-5}$ RIU. The highest FOM was achieved with Au_Ag NPs (16%), which is 1.95×10^{13} μm $(\text{RIU}\bullet^\circ)^{-1}$, which is 7 orders of magnitude greater than that of the pure Au substrate.

Calibration of the plasmonic biosensing substrate

The comparison of reflectivity curves between the pure Au substrate, often considered as standard reference for bio-detection, and the Au_Ag NPs (16%) sensing substrate architecture at a wavelength of 785 nm is shown in Fig. 6a. Both the experimental and simulation results showed that the SPR reflectivity can be significantly reduced at an Ag NPs concentration of 16%. To calibrate the refractometric performance of the sensor, glycerin solutions with weight ratios from 0.1% to 2.5% were flowed to the sensor flow microchannel with a fixed refractive index change. The real-time differential GH shift measurements at 785 nm, induced by glycerin solutions with increasing weight ratios, was shown in Fig. 6b. Both substrates exhibit an increasing GH shift with increasing glycerin weight ratios, and the maximum GH shift was measured at 554.3 μm for Au_Ag NPs (16%) substrate. Moreover, the Au_Ag NPs (16%) substrate consistently shows a significantly larger shift than the pure Au substrate at all concentrations. For example, for the glycerin solution with a low weight ratio of 0.5%, the Au_Ag NPs (16%) sensing substrate could generate GH shift of around 200.8 μm, which is more than 4 times that of the pure Au substrate (39.5 μm). This enhanced response highlights that the incorporation of Ag NPs

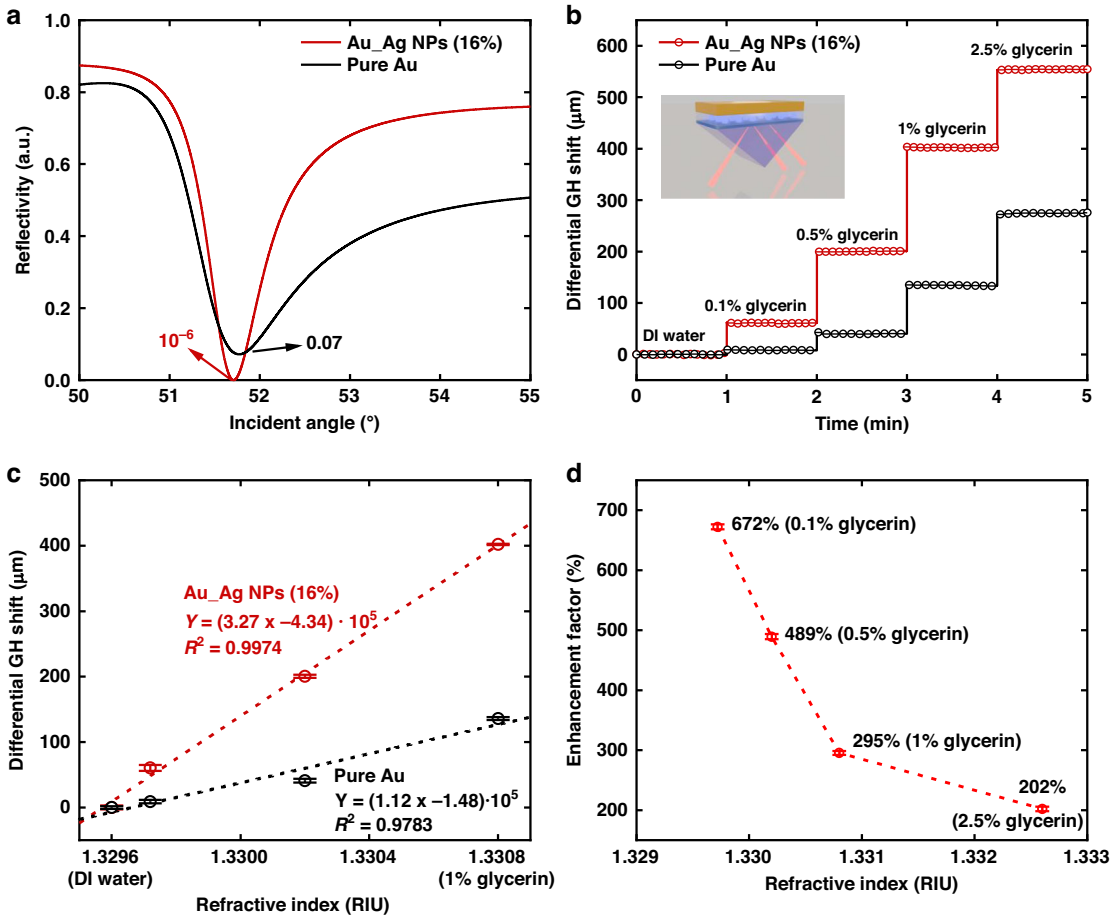

Fig. 6 Calibration of the Au_Ag NPs (16%) sensing substrate. a The analytical reflectivity curves of pure Au (black curve) and Au_Ag NPs (16%) (red curve) substrate at 785 nm. **b** Real-time observation of the GH shift caused by varying glycerin concentrations (0.1%, 0.5%, 1% and 2.5%) performed on both pure Au (black curve) and Au_Ag NPs (16%) (red curve) substrates at 785 nm. **c** Linear fitting of differential GH shift versus refractive index changes for pure Au and Au_Ag NPs (16%) substrates. **d** The enhancement factor between Au_Ag NPs (16%) and pure Au substrates at different glycerin concentrations (0.1%, 0.5%, 1% and 2.5%)

amplifies the sensitivity of the plasmonic resonance, improving the sensor's ability to detect minute variations in refractive index.

The GH shift, measured as a function of refractive index using glycerin solutions, is summarized in Fig. 6c. It is well known that each 0.1% increment in glycerin weight ratio corresponds to a refractive index change of 0.00012 RIU[37]. Calibration experiments were performed on both pure Au and Au_Ag NPs (16%) substrates at a wavelength of 785 nm, with each measurement repeated three times to ensure reproducibility. As shown by the dashed lines in Fig. 6c, the sensitivity was determined through the linear analysis of calibration data. Experimental results demonstrated that the sensing substrates with low reflectivity at the resonance angle exhibited significantly enhanced sensitivity. Specifically, the Au_Ag NPs (16%) substrate achieved a sensitivity value of 3.27×10^8 nm RIU^{-1} at 785 nm, representing a twofold improvement over the pure Au substrate. With a position resolution of 0.12 μm, the plasmonic biosensor platform achieved a refractive index resolution of 3.67×10^{-7} RIU. Furthermore, Fig. 6d illustrates the enhancement factor between the Au_Ag NPs (16%) and pure Au substrates at different glycerin weight ratios. It is worth noting that the enhancement factor reached more than 670% at 0.1% of glycerin.

Detection of small biological molecules

To test the ability of this sensor platform to detect small biological molecules in extremely diluted solutions, biotin was used in this work. Biotin is a small molecule for calibration performance with a low molecular weight of 244 Da, as shown in the inset of Fig. 7b. Conventional SPR-based biosensor techniques are not capable to obtain a detectable response even with a high concentration of 100 μM. In contrast, previous studies achieved biotin detection capabilities down to 10 μM with plasmonic

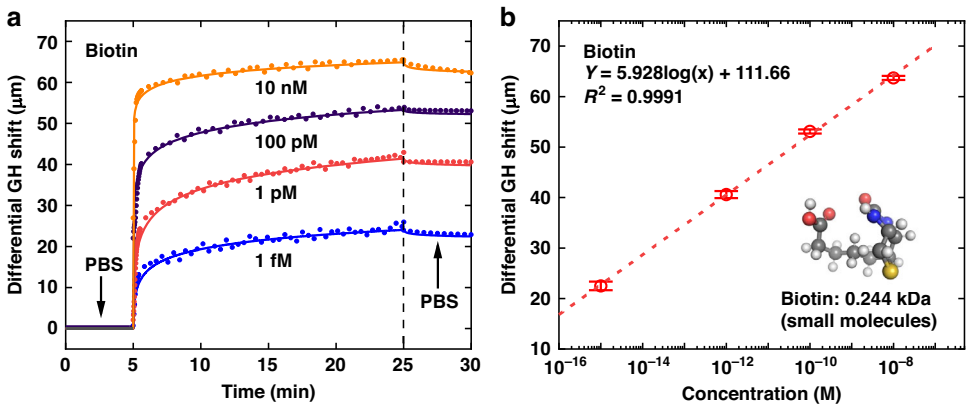

Fig. 7 Streptavidin-biotin sensing test. a Real-time monitoring of the differential GH shift for biotin at concentrations from 1 fM to 10 nM, using a streptavidin-functionalized surface on the Au_Ag NPs (16% in Al_2O_3) plasmonic biosensing substrate. **b** Linear fitting of the differential GH shift, demonstrating the relationship between the GH shift and biotin concentration. The slope of the fitted line represents the sensitivity of the biosensing platform. Each data point represents the average value of 3 individual measurements, and the error bars correspond to the standard deviation

nanorod metamaterials[16] and 10 pM with hyperbolic metamaterials[17] by using a conventional streptavidin-biotin binding assays. Notably, our sensor substrate Au_Ag NPs (16%) demonstrated four orders of magnitude more sensitivity than the hyperbolic metamaterials, achieving the real-time binding monitoring of 1 fM biotin in phosphate buffered saline (PBS).

Biotin was characterized by its low isoelectric point of 3.5, carrying a strong negative charge under neutral buffer conditions[38]. To validate the use of a well-defined affinity pair, biotin detection using a streptavidin-functionalized surface is carried out (Fig. S8). The GH shift is recorded during PBS injection and followed for various concentrations of biotin (1 fM to 10 nM) in real-time during an adsorption time of 20 min. The real-time response of the sensor during the injection of 1 fM biotin is shown in the Fig. 7a. The differential GH shift after 20 minutes of 1 fM biotin adsorption was measured to be 23.9 μm. Finally, a small drop in GH shift (22.5 μm) was obtained by injecting PBS in the microfluidic channel again to remove the unbound biotin molecules. In addition, to demonstrate the repeatability of the sensing response, three individual measurements were performed at different concentration. Figure S11 shows representative real-time sensorgram from repetitions for 1 fM biotin. The performance of the sensor is shown in the Fig. 7b, which plots the GH shift with different concentrations. It revealed a significant signal increase of 5.9 μm per order of magnitude change in biotin concentration showing that the sensor substrate was extremely sensitive to the tiny refractive index change.

Detection of cancer markers

The clinical applicability of the proposed biosensing platform was validated by demonstrating its capability to detect cancer biomarkers with ultrahigh sensitivity. Tumor necrosis factor-alpha (TNF-alpha), a cytokine with a molecular weight of 17.3 kDa, was selected as the target analyte. The measurements were performed using the same Au_Ag NPs (16%) substrate previously employed for glycerin calibration and small biomolecule detection at a wavelength of 785 nm. To enable specific detection of TNF-alpha, the sensing substrate was functionalized with an aptamer specifically designed for TNF-alpha capture and then followed with mPEG-SH for blocking the remaining Au surface without the aptamer (Fig. S9). An AFM measurement on clean regions of the chip shows a step height of 6 nm between bare Au and functionalized areas (Fig. S10), confirming the presence of a nanoscale aptamer layer. This thickness is consistent with reported values for densely packed thiolated ssDNA aptamer monolayer on gold. Based on the classical studies[39,40], the corresponding aptamer surface density on sensing region ($10 \times 10\ mm^2$) is evaluated at $3 \times 10^2\ pg/mm^2$.

Figure 8a illustrates the real-time sensor response to TNF-alpha at an ultra-low concentration of 0.1 aM, which is four orders of magnitude compared to a surface-enhanced Raman spectroscopy substrate by using gold nanoparticles[41]. The incubation process lasted 20 min, followed by flushing with a running buffer. At this concentration, the measured differential GH shift was around 3.3 μm. Notably, the signal continued to increase for over 10 minutes, reflecting the slow binding kinetics at such trace levels. Figure 8b presents the GH shift of TNF-alpha detection across a concentration range from 1 aM to 1 pM. As the biomarker concentration increased, the signal shift after buffer flushing became more pronounced, and the time required to reach signal saturation decreased significantly. For instance, at 1 pM, signal saturation was achieved within 1 minute, compared to the prolonged

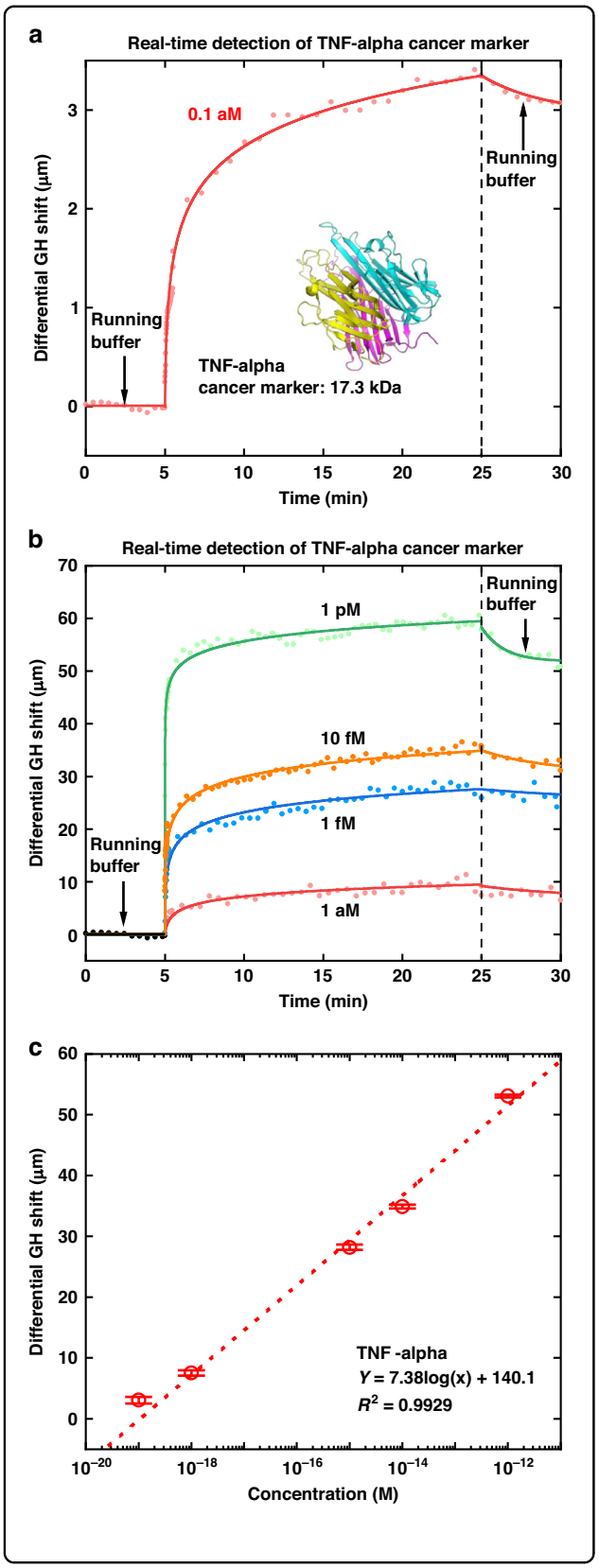

Fig. 8 Specific detection of biomarkers using aptamer-functionalized plasmonic biosensing substrate. a Real-time monitoring of the cancer marker TNF-alpha at an ultra-low concentration of 0.1 aM on the Au_Ag NPs (16% in Al_2O_3) sensing substrate. **b** Real-time detection of TNF-alpha across a wide range (1 aM to 1 pM) on the Au_Ag NPs (16%) substrate. **c** Linear fitting analysis of the sensor response to TNF-alpha concentrations, illustrating the quantitative relationship between the signal and TNF-alpha concentration. Each data point represents the average value of three individual measurements, and the error bars correspond to the standard deviation

response observed at 0.1 aM. The concentration of TNF-alpha in the blood serum of cancer patients typically ranges from 20 to 50 pg mL^{-1}, corresponding to approximately 10^{-13} M in early-stage cancer. As shown in Fig. 8c, linear fitting analysis of the sensor response revealed a differential GH shift of 46.8 μm at 10^{-13} M TNF-alpha concentration. In addition, to demonstrate the good repeatability of our experiments, we have repeated the targeted biosensing experiments by 3 times. The error bars based on these 3 measurements have been plotted in Fig. 8c show a ± 0.25 μm even for the low concentration for 0.1 aM of TNF-alpha biomarkers. Figure S12 shows representative real-time sensorgram from the second and third repetitions for 0.1 aM, 1 fM and 1 pM, respectively. These results demonstrate that the biosensing platform achieves the stable sensitivity required for early-stage cancer diagnostics, highlighting its potential for clinical applications in biomarker detection.

Selectivity test for different cancer markers

To further evaluate the selectivity of the plasmonic biosensor, we investigated its response to both target-specific (TNF-alpha) and non-specific (Interleukin-6, IL-6) cytokines at a concentration of 10 fM. The sensing substrate was functionalized with TNF-alpha-specific aptamers to ensure selective binding of the target analyte. As depicted in Fig. 9, the biosensor exhibited a robust response of 32.4 μm for 10 fM TNF-alpha, reflecting the high affinity of the aptamer-functionalized surface for its target molecule. In contrast, a significantly weaker response of 0.5 μm to non-specific 10 fM IL-6 adsorption was observed, highlighting the sensor's ability to discriminate between specific and non-specific interactions. Furthermore, after flushing with a running buffer, the signal corresponding to IL-6 returned to near-baseline levels, indicating the absence of strong binding between the non-specific cytokine and the functionalized substrate. In comparison, the TNF-alpha signal showed only a minimal reduction, further confirming the high selectivity and binding stability of the aptamer-functionalized sensing substrate. Besides, we also observed the same trend at

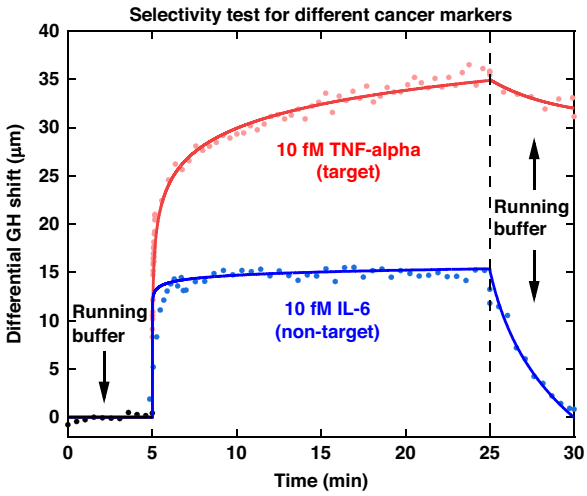

Fig. 9 Selectivity test for different cancer markers. Real-time detection of 10 fM TNF-alpha cancer marker (target) and IL-6 (Non-target) on Au_Ag NPs (16% in Al_2O_3) sensing substrate functionalized by TNF-alpha aptamers

low concentrations of 1 fM (Fig. S13). The signal reaches a quasi-steady state within 6 min(Fig. S13). This confirms that the platform exhibits stability under different operating conditions. In addition, the blocking efficiency is functionally confirmed by the selectivity experiments. For example, at 1 fM (Fig. S13), the specific target TNF-alpha produces a large and stable response (25 μm) after rinsing, whereas the non-target IL-6 at the same concentration gives only 1 μm response, after running buffer rinsing. This indicates that nonspecific IL-6 molecules adsorption on the TNF-alpha aptamer-mPEG-SH-functionalized surface is strongly suppressed. This confirms that the platform exhibits stability under operating conditions. These results underscore the sensor's potential for accurate and reliable detection of target analytes in complex biological samples, even in the presence of potential interferents.

Simulation analysis of GH shift enhanced by Ag NPs

Figure 10a shows the electric field distribution inside the multilayer structure under SPR conditions. The incident Gaussian beam (with a beam width of 3 μm) propagates from the substrate side and undergoes total internal reflection at the metal-dielectric interface where most of the incident beam is absorbed leading to a dark band at the reflection side. A portion of the electromagnetic wave penetrates the metal layer due to the evanescent field and re-emerges inside the substrate. A lateral displacement of the reflected beam is then observed relative to the incident beam path: GH shift. We used a numerical finite-difference time-domain (FDTD) method to simulate the electromagnetic field interactions with the surface plasmon. The model consists of an incident plane wave propagating from a BK7 glass (incident plane) to the Al_2O_3-Au substrate, with or without Ag NPs randomly embedded within a Al_2O_3 matrix (12 nm). For both cases, the SPR condition angle was determined by plotting the reflected wave intensity as a function of the incident angle of the plane wave, with the resonance angle defined as the point at which the reflection reached its minimum value. The impact of Ag NPs on the SPR phase response is investigated by plotting the phase map of the reflected wave. The phase map at the SPR resonance angle for the structure without nanoparticles (Fig. 10b) serves as the baseline. A comparison with the phase map for the Au_Ag NPs substrate demonstrates a modulation of the phase wavefront of the reflected plane wave at the resonance angle (Fig. 10c). This effect does not appear at an incident angle out of the resonance angle, nor at the resonance angle for the structure without NP. The impacts of Ag NPs induced modulations of the wave-front phase on the GH shift are calculated by monitoring the phase of the reflected wave, at a single mesh point located in the reflection region, versus the angle of the incident plane wave. This approach enables a direct assessment of how the phase evolves near the resonance condition and is particularly useful for evaluating the sensitivity of the system. Figure 10d shows that the phase shift at resonance for the structure with nanoparticles is sharper than that for the structure without nanoparticles. The phase change was calculated over an angular step of 0.01° near the resonance angle for both structures. The structure incorporating nanoparticles exhibited a phase variation 4 times higher than that of the reference structure without nanoparticles. This sharper phase change in the nanoparticle-incorporated structure indicates an increase in phase sensitivity, leading to a much larger GH shift.

In addition, the electromagnetic field distribution in the designed plasmonic biosensor structure exhibits different characteristics under resonant and non-resonant conditions (Fig. S14). Under surface plasmon resonance excitation, a strong localized field appears at the interface between the gold layer and the silver nanoparticle-doped dielectric medium, indicating effective coupling between the localized surface plasmon mode and the propagating surface plasmon mode. This hybrid plasma state generates a confined electromagnetic field with a steep phase gradient, which fundamentally leads to the observed phase and singularities GH shift. In contrast, simulations under non-resonant conditions show significantly reduced field strengths, but we observe strong near-field coupling between ultra-small silver nanoparticles, resulting in coherent collective plasmon modes. Moreover, the effect of a single Ag NP on the electric field was also considered, as shown in the Fig. S15, achieving approximately an order-of-magnitude amplification compared to the pure Au film.

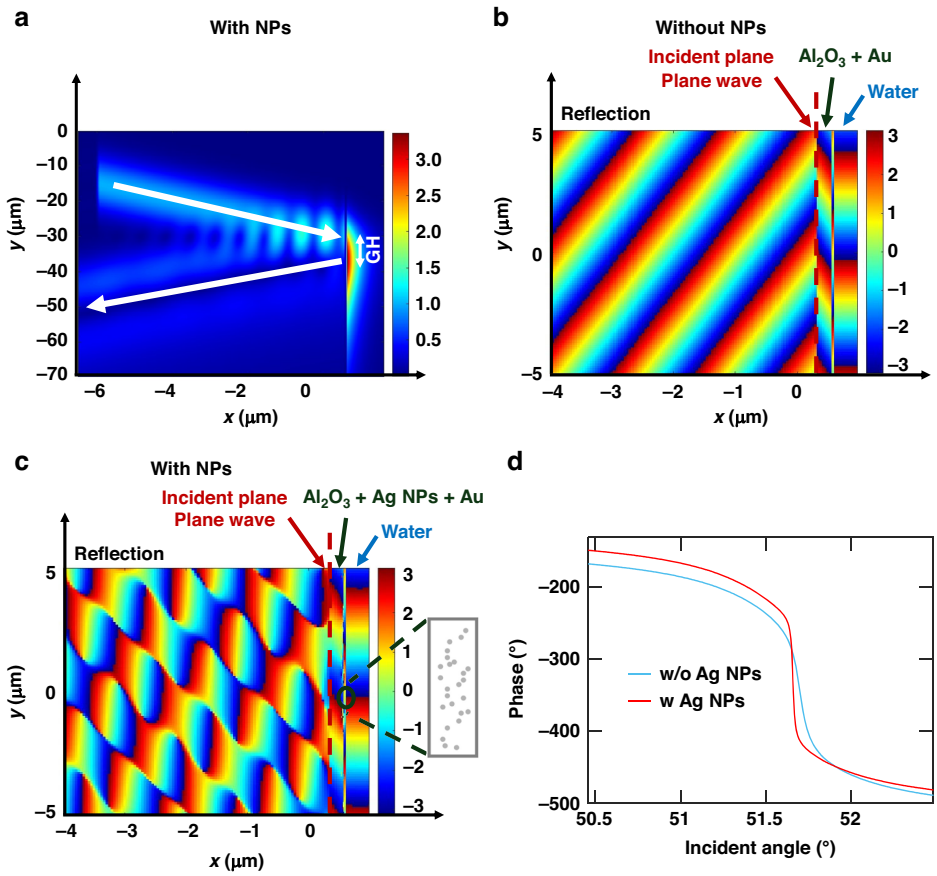

Fig. 10 FDTD simulations on a 48 nm Au layer, 12 nm Al_2O_3 and 2.3 nm diameter Ag NPs. a Simulation of a Gaussian beam (width = 3 μm) incident on at the SPR resonance angle. **b** Phase maps of the incident and reflect plane wave (λ = 785 nm) at the SPR resonance angle without nanoparticles. **c** Phase maps of the incident and reflect plane wave at the SPR resonance angle with nanoparticles. **d** Phase shift of the reflection plan wave (λ = 785 nm) as a function of incident angle for the structure with and without nanoparticles

To highlight the benefits of using silver nanoparticles in an Al_2O_3 matrix, additional FDTD simulations were performed. As shown in Fig. S16a, Ag NPs induce a much deeper SPR reflectivity dip ($\sim 1 \times 10^{-3}$), with a minimum reflectance nearly seven times lower than with Au NPs ($\sim 7 \times 10^{-3}$). They also produce a significantly stronger phase modulation of the reflected wave (Fig. S16b,c). Since only the NP material differs, these results clearly demonstrate the superior ability of Ag NPs to enhance light coupling and improve phase-based sensitivity, that leads to enhanced GH shifts.

As shown in Fig. S17a, the Al_2O_3 matrix leads to a pronounced SPR dip, reducing the minimum reflectance by a factor of four compared to SiO_2 and ten compared to air. This enhanced response arises from the higher permittivity of Al_2O_3 at 785 nm ($Re(\varepsilon_i) = 3.1184$), consistent with Mie theory resonance conditions. In this configuration, part of the electromagnetic field interacts with the embedded NPs while the remainder couples to the surface plasmon waves. Phase-map simulations (Fig. S17b–e) further reveal the strongest phase modulation at resonance for Ag NPs in Al_2O_3 compared to other matrixes, highlighting the substantial role of the Ag NPs and Al_2O_3 combination on the overall optical response.

Discussion

In this study, we developed a novel plasmonic biosensor based on nanocomposite thin films that exploits extreme optical phase singularities and GH shift for ultrasensitive, label-free detection. For the first time, we precisely arranged sub-3 nm Ag NPs arrays within a 12 nm Al_2O_3 dielectric matrix via layer-by-layer configuration and integrated them with a 48 nm gold film to form a hybrid plasmonic structure. This design achieves a dual enhancement mechanism: (i) strong near-field coupling between ultra-small Ag NPs, generating coherent collective plasmon modes; and (ii) synergistic interactions between the localized surface plasmon resonance (LSPR) of the nanoparticles and the surface plasmon polaritons (SPPs) in the gold film. The resulting nanoscale optical

cavity exhibits sharp phase singularities, which significantly amplifies the GH shift response to small refractive index changes.

The sensor is optimized for the red to near-infrared region (785 nm) and achieves an excellent refractive index sensitivity of 3.27×10^8 nm/RIU, with a maximum lateral GH shift of 554.3 μm in 2.5% glycerol solution. Its linear dynamic range covers clinically relevant concentrations, enabling real-time quantitative analysis. The phase singularity-enhanced sensing mechanism stems from the interaction between the SPP of the gold film (providing directional excitation) and the LSPR of the silver nanoparticle array (generating local field hot spots). Near the "dark spot" (reflectivity reached to quasi-zero), these effects generate a steep phase gradient that converts small refractive index changes into measurable GH shifts.

To validate its biomedical application, the sensor was functionalized with a TNF-alpha-specific aptamer, achieving the lowest detectable concentration of 0.1 aM. Selective testing against IL-6 confirmed its stability, with a GH shift of 32.4 μm for TNF-alpha and 0.5 μm for IL-6, indicating minimal cross-reactivity. The sensor outperforms conventional plasmonic sensors by utilizing dual-mode enhancement (SPP + LSPR) and phase-singularity effects of sub-3 nm nanoparticle arrays.

The platform's label-free operation, ultra-low detectable concentration, and high specificity make it ideal for point-of-care diagnostics. Future studies will focus on clinical translation, including multiplexed detection and integration with microfluidics. The nanoparticle array-driven phase control strategy opens new avenues for quantum plasmonic biosensing at the sub-nanometer scale.

Materials and methods

Pulsed laser deposition

Gold and Al_2O_3 thin films are deposited using the Pulsed Laser Deposition (PLD) method (Fig. S18a). A pulsed KrF excimer laser (Light Machinery IPEX 742, $\lambda = 248$ nm, pulse width 25 ns) is focused on a target material. The light-matter interaction results in the generation of a highly orientated plasma plume composed of electrons, radicals and ions coming from the target. The vapor-phase species undergoes an adiabatic expansion followed by a condensation onto the substrate, positioned in front and parallel to the target, at a distance of 5 cm. Soda-lime glass slides of $2.5 \times 2.5\ cm^2$ are used as the deposition substrate. The slides are ultrasonically cleaned in acetone, ethanol, flushed with deionized water and dried with argon, prior to deposition. Deposition over uncommon large-area substrates size is achieved through substrate rotation, controlled laser scanning over the target and off-axis deposition. The whole process is carried out in an ultra-high vacuum chamber with a base pressure of 5×10^{-8} mbar, ensuring an accurate control over atmosphere and pressure. PLD was chosen for its ability to produce high quality, dense thin films and congruent transfer from the target to the film without needing additional heating of the substrate. Also, PLD offers the capacity of controlling the kinetic energy and the deposition rate at the atomic scale, enabling an accurate control of the grown thin film thickness, which is a critical parameter for plasmonic applications. The parameters used in this work are detailed in Table S1. Particularly, in the case of gold, to avoid the liquid droplets ejection from the target, PLD was operating at a relatively low fluence, close to the threshold ablation fluence which is around 1.6 $J.cm^{-2}$ using a KrF laser[42].

Nanoparticles generator

The silver nanoparticles have been synthetized using a free cluster generator developed by our group and described elsewhere[25]. A cross-section-view of the generator is presented in the Fig. S18b. The working principle is derived from Smalley's and Milani-deHeer's source[43,44]. The ablation of a target by a Nd:YAG laser (Q-Switched Spectra Physics Quanta Ray INDI, 2ω, $\lambda = 532$ nm, pulsed duration 7 ns) creates a plasma plume that expands inside a nucleation chamber. This small cavity is closed on one side by the target and the laser entrance window on the other. Each laser pulse is followed by the aperture of a synchronized pulsed valve, which allows the introduction of high-pressure (10 bar) helium puffs. The aperture duration determines the amount of helium introduced, and thus the relative pressure and the residence time of the vapor inside the nucleation chamber. The laser pulses and the valve aperture are synchronized via a delay generator (Stanford Research Systems DG535, with 1 ns accuracy). The helium gas leads to the quenching of the freshly formed plasma plume, composed of species evaporating from the target. Supersaturated conditions are reached, inducing the formation of nuclei and the growth of the nanoparticles. The mixture, gas and nanoparticles, then undergo a supersonic expansion through a nozzle directed towards the UHV PLD chamber. Inside the main chamber, this expansion is adiabatic, and the probability of having aggregates-aggregates or atoms-aggregates collisions becomes very low and the particles size can be considered fixed at the exit of the nozzle. The silver clusters are deposited on the substrate placed at a distance of 37 cm from the exit of the nozzle, with an angle of 45° regarding the particles' flow, in the main chamber. To achieve a homogeneous deposition, the substrate holder is rotated at 3 rpm. The kinetic energy reached by the silver nanoparticles is estimated to be around 0.14 eV/atom, which is 20 times lower than the cohesive energy of silver (2.95 eV/atom). This deposition regime, sometimes called "Low Energy Cluster Beam Deposition" (LECBD), should prevent clusters fragmentation during their impact on the

substrate[45]. The in-flight size and structure of most of the silver nanoparticles should therefore be kept[46]. Using the nanoparticles generator and/or the PLD either separately, simultaneously or sequentially results in nanoparticles stacks, nanocomposite thin films with embedded nanoparticles or multilayered nanoparticles-thin film structures, respectively. The advantage of this setup is the development of new nano-architectures with exotic properties in a single reactor, without any contamination at the interface. The experimental control conditions can produce clusters with sizes in the range 1-10 nm and a relatively monodisperse size distribution. Tuning the size of nanoparticles can be achieved by adjusting several parameters such as the helium pressure, the laser-valve synchronization delay, the laser fluence, the nozzle design and the aperture duration of the pulsed valve. Table S2,3 reports the parameters used to synthetize silver nanoparticles in this work. In these conditions, the deposition rate is very low, around 0.2 nm per minute (4 Hz), and is therefore accurately controlled using a Quartz Crystal Microbalance (Maxtek inc., TM-400, sensitivity of 0.1 $Å.s^{-1}$). The effective error (± %) of the Ag NPs concentration was determined to be ± 2% Vol by precisely monitoring the deposition rate with a quartz crystal microbalance (QCM). The stability of the nanoparticle flux is also regularly monitored by depositing the particles onto TEM grids. TEM analysis provides accurate control of both nanoparticle size and surface coverage.

Chemicals

The following chemicals were purchased from Sigma-Aldrich, France: absolute ethanol, sodium chloride (NaCl), magnesium chloride ($MgCl_2$), biotin, streptavidin, (3-Amino-Propyl) trimethoxy silane (APTMS), Interleukin-6 (IL-6), tumor necrosis factor alpha (TNF-alpha), and glycerin. mPEG-SH (MW: 350 Da) was sourced from Creative PEGWorks, while phosphate-buffered saline (PBS, pH 7.4) was acquired from Thermo-Fisher, France. Ultrapure water, purified using a PURELAB Flex system (Veolia Water Technologies), was used throughout the experiments.

DNA aptamers

The TNF-alpha specific DNA aptamer (5'-TGGTGGATGGCGCAGTCGGCGACAA-3'), modified with a 5' thiol group, was procured from Microsynth AG (Switzerland). A stock solution (100 µM) was prepared in running buffer (1× PBS, pH 7.4) containing 1 mM $MgCl_2$ for subsequent experiments.

Bio-sample preparation

A series of glycerin solutions (0.1%, 0.5%, 1%, and 2.5% (w/v)) were prepared in ultrapure water. Biotin was dissolved to a 0.1 mM stock solution, followed by sterile filtration (0.2 µm syringe filter) and subsequent serial dilution (1 fM–10 nM). Streptavidin was dissolved to a 1 mg/mL stock solution and further diluted to 1 µM for surface functionalization. APTMS and mPEG-SH were each diluted to 1 mM in PBS and running buffer, respectively. Recombinant TNF-alpha was reconstituted to a stock concentration of 0.5 $mg\,mL^{-1}$ and further diluted in running buffer to working concentrations ranging from 0.1 aM to 1 nM. The thiol-modified TNF-alpha aptamer, provided as a lyophilized powder (0.5 $mg\,mL^{-1}$ upon reconstitution), was diluted to 1 nM in running buffer prior to use.

Sensing substrate functionalization

The Au surface of the Au_Ag NPs (16%) substrate was functionalized with various linkers to enable selective biomolecule detection. Prior to functionalization, the sensing substrate was sequentially cleaned with absolute ethanol and ultrapure water, then mounted on the translation stage. For biotin detection, the substrate was incubated with 1 µM streptavidin for at least 1 h to facilitate surface modification.

In the case of TNF-alpha detection, TNF-alpha specific aptamers were introduced to covalently bind the Au surface, with real-time monitoring until signal stabilization. Unbound aptamers were removed by rinsing with 1 mL of running buffer, followed by GH shift measurement. After solution removal, a second injection of running buffer established the post-functionalization baseline. Surface blocking was performed using mPEG-SH under identical conditions to aptamer immobilization, with subsequent buffer injection serving as the reference baseline for subsequent biomolecular assays.

Before performing the specificity measurements, the sensing platform was first calibrated using deionized water, glycerin at different concentrations, and the running buffer to determine the optimal SPR operating point and to ensure that the resonance dip was properly positioned within the maximum sensitivity region. Subsequently, the sensor chip was functionalized by immobilizing the TNF-alpha aptamer onto the gold surface, followed by using mPEG-SH to block the remaining unmodified areas and suppress nonspecific adsorption. For the specificity experiments, the two biomolecules were injected sequentially. First, the non-target biomolecule IL-6 was first injected and incubated for 20 min until the optical signal reached stable. The sensor surface was then rinsed with the running buffer to remove unbound molecules, and the signal was monitored until a stable baseline was re-established. Immediately after, the target biomolecule TNF-alpha was injected under identical conditions and incubated for 20 min until signal stabilization was achieved. A subsequent rinsing step with the running buffer was again performed to eliminate non-specifically bound species and to ensure that the recorded

response corresponded exclusively to specific binding. This sequence ensures that the responses correspond to distinct binding events without cross-interference.

Analytical modeling of the nanocomposite sample

Finite-Difference Time-Domain (FDTD) simulations were performed using Lumerical software to model the interaction of light with surface plasmon. The model consists of a plane wave ($\lambda = 785$ nm) propagating inside a gold layer (48 nm) on a dielectric substrate, with spherical silver nanoparticles (2.3 nm diameter) embedded within an Al_2O_3 matrix (12 nm thickness). The spherical nanoparticles were randomly positioned into the Al_2O_3 matrix, ensuring a uniform distribution throughout. The nanoparticle concentration (f) was defined, and the required number of nanoparticles to be added in the Al_2O_3 matrix before the simulation was calculated based on the volume of the Al_2O_3 matrix and the volume of a single nanoparticle using the following formula:

$$Number\ of\ Nanoparticles = \frac{f \times Volume\ of\ alumina}{Volume\ of\ 1\ NP}$$

To prevent particle overlap, a spatial constraint was applied, ensuring that the distance between any two nanoparticles was always larger than twice the nanoparticle radius (1.15 nm).

The simulation domain was bounded by Perfectly Matched Layer (PML) boundary conditions in the x-direction to absorb outgoing waves and minimize reflections, while Bloch boundary conditions were applied in the y-direction. The mesh size in the Al_2O_3 matrix was set to 1/1000 of the nanoparticle radius to ensure fine resolution of the electromagnetic field distributions around the nanoparticles.

A 2D field monitor was placed within the simulation domain to record the electric field distribution across the SPR structure. The source is launched at 150 nm above the metal–substrate interface. To avoid interference effects between the incident and reflected waves, the reflected signal is monitored at a distance longer than 150 nm above the metal-substrate interface. The incident angle of the plane wave varied with a resolution of 0.01° to obtain electric field data at multiple angles, ensuring high precision in the phase shift analysis. The phase was then obtained by calculating the angle of the complex electric field, which provides the phase shift as a function of the incident angle.

Acknowledgements

This work is supported under the UTT Project Stratégique NanoSPR (OPE-2022-0293), the Graduate School (Ecole Universitaire de Recherche) "NANOPHOT" (ANR-18-EURE-0013), the project Sigma PIX from the laboratory of excellence, LabEx Sigma-lim ANR-10-LBX-0074, launched by the French Ministry of Higher Education and Research (https://www.unilim.fr/labex-sigma-lim) between IRCER (https://www.ircer.fr) and the XLIM (https://www.xlim.fr) Research Institutes, and funded by the ANR (French Research Agency) project WideSensing (ANR-25-CE42-5720). Financial support of Nano'Mat (http://www.nanomat.eu) by the Ministère de l'enseignement supérieur et de la recherche, the Conseil régional Grand Est, the FEDER fund, and the Conseil général de l'Aube are also acknowledged. The authors would like to thank Valérie Coudert, Pierre Carles and Etienne Laborde at the characterization platform CARMALIM (https://www.unilim.fr/carmalim/), for AFM, FIB and TEM experiments, and XPS analyses respectively.

Author details

[1]Light, Nanomaterials & Nanotechnologies (L2n), CNRS-UMR 7076, University of Technology of Troyes, 10004 Troyes, France. [2]Institute of Research for Ceramics (IRCER), CNRS-UMR 7315, University of Limoges, 87000 Limoges, France. [3]Research Institute of XLIM, CNRS-UMR 7252, University of Limoges, 87000 Limoges, France. [4]ALPhANOV, Centre technologique Optique & Lasers, 87280 Limoges, France. [5]European University of Technology Institute of Nanomaterials and Nanotechnologies (EUTINN), European University of Technology, European Union, Troyes 10004, France

Author contributions

G.H., F.D.B., C.C., and S.Z. conceived the idea and designed the research. F.D., M.G., J.Y., G.H., F.D.B., C.C., and S.Z. designed, fabricated, and characterized the samples. F.D., J.Y., G.H., and S.Z. performed sensing experiments and carried out calculations and simulations. F.D., M.G., F.D.B., C.C. and S.Z. designed the biological protocols and surface modifications and surface characterization experiments. F.D., M.G., G.H., S.V., F.D.B., C.C., and S.Z. wrote the manuscript based on the input from all authors. S.Z., C.C., F.D.B., S.V., and G.H. supervised the project. All authors analyzed the data and discussed the results.

Data availability

The authors declare that the data supporting the findings of this study are available within the paper and its Supplementary Information files. Should any raw data files be needed in another format they are available from the corresponding author upon request.

Conflict of interest

The authors declare no competing interests.

Supplementary information The online version contains supplementary material available at https://doi.org/10.1038/s41378-026-01222-3.

Received: 17 September 2025 Accepted: 31 January 2026
Published online: 25 March 2026

References

1. Barth, I. & Lee, H. Nanophotonic sensing and label-free imaging of extracellular vesicles. *Light Sci. Appl* **14**, 177. https://doi.org/10.1038/s41377-025-01866-2 (2025).
2. Shaked, N. T., Boppart, S. A., Wang, L. V. & Popp, J. Label-free biomedical optical imaging. *Nat. Photonics* **17**, 1031–1041, https://doi.org/10.1038/s41566-023-01299-6 (2023).
3. Chen, C. et al. Evanescent wave-based optical biosensors for innovations, medical application and future perspectives. *J. Adv. Res* https://doi.org/10.1016/j.jare.2025.07.007 (2025).
4. Minopoli, A. et al. Ultrasensitive antibody-aptamer plasmonic biosensor for malaria biomarker detection in whole blood. *Nat. Commun.* **11**, 6134. https://doi.org/10.1038/s41467-020-19755-0 (2020).
5. Zhao, Z. et al. Nanocaged enzymes with enhanced catalytic activity and increased stability against protease digestion. *Nat. Commun.* **7**, 10619. https://doi.org/10.1038/ncomms10619 (2016).
6. Jung, J. K. et al. Cell-free biosensors for rapid detection of water contaminants. *Nat. Biotechnol.* **38**, 1451–1459, https://doi.org/10.1038/s41587-020-0571-7 (2020).
7. Del Villar, I. et al. Nano-Photonic Crystal D-Shaped Fiber Devices for Label-Free Biosensing at the Attomolar Limit of Detection. *Adv. Sci. (Weinh.)* **11**, e2310118. https://doi.org/10.1002/advs.202310118 (2024).
8. Zu, L. et al. Ultrasensitive and Multiple Biomarker Discrimination for Alzheimer's Disease via Plasmonic & Microfluidic Sensing Technologies. *Adv. Sci. (Weinh.)* **11**, e2308783. https://doi.org/10.1002/advs.202308783 (2024).

9. Santano, D., Socorro, A. B., Giannetti, A., Villar, I. D. & Chiavaioli, F. Simultaneous detection of inflammatory process indicators via operando dual lossy mode resonance-based biosensor. *Opto-Electronic Science* **4**, https://doi.org/10.29026/oes.2025.250005 (2025).
10. Barth, I., Conteduca, D., Reardon, C., Johnson, S. & Krauss, T. F. Common-path interferometric label-free protein sensing with resonant dielectric nanostructures. *Light Sci. Appl* **9**, 96. https://doi.org/10.1038/s41377-020-0336-6 (2020).
11. Needham, L.-M. et al. Label-free detection and profiling of individual solution-phase molecules. *Nature* **629**, 1062–1068, https://doi.org/10.1038/s41586-024-07370-8 (2024).
12. Kabashin, A. V., Kravets, V. G. & Grigorenko, A. N. Label-free optical biosensing: going beyond the limits. *Chem. Soc. Rev.* **52**, 6554–6585, https://doi.org/10.1039/d3cs00155e (2023).
13. Zeng, S., Baillargeat, D., Ho, H.-P. & Yong, K.-T. Nanomaterials enhanced surface plasmon resonance for biological and chemical sensing applications. *Chem. Soc. Rev.* **43**, 3426–3452 (2014).
14. Lee, J. et al. Plasmonic biosensor enabled by resonant quantum tunnelling. *Nat. Photonics* https://doi.org/10.1038/s41566-025-01708-y (2025).
15. Altug, H., Oh, S.-H., Maier, S. A. & Homola, J. Advances and applications of nanophotonic biosensors. *Nat. Nanotechnol.* **17**, 5–16, https://doi.org/10.1038/s41565-021-01045-5 (2022).
16. Kabashin, A. V. et al. Plasmonic nanorod metamaterials for biosensing. *Nat. Mater.* **8**, 867–871, https://doi.org/10.1038/nmat2546 (2009).
17. Sreekanth, K. V. et al. Extreme sensitivity biosensing platform based on hyperbolic metamaterials. *Nat. Mater.* **15**, 621–627, https://doi.org/10.1038/nmat4609 (2016).
18. Jahani, Y. et al. Imaging-based spectrometer-less optofluidic biosensors based on dielectric metasurfaces for detecting extracellular vesicles. *Nat. Commun.* **12**, 3246. https://doi.org/10.1038/s41467-021-23257-y (2021).
19. Kravets, V. G. et al. Singular phase nano-optics in plasmonic metamaterials for label-free single-molecule detection. *Nat. Mater.* **12**, 304–309, https://doi.org/10.1038/nmat3537 (2013).
20. Sreekanth, K. V. et al. Biosensing with the singular phase of an ultrathin metal-dielectric nanophotonic cavity. *Nat. Commun.* **9**, 369. https://doi.org/10.1038/s41467-018-02860-6 (2018).
21. Zeng, S. et al. Graphene-gold metasurface architectures for ultrasensitive plasmonic biosensing. *Adv. Mater* **27**, 6163–6169 (2015).
22. Oh, S.-H. et al. Nanophotonic biosensors harnessing van der Waals materials. *Nat. Commun.* **12**, 3824. https://doi.org/10.1038/s41467-021-23564-4 (2021).
23. Barth, I. & Lee, H. Phase-driven progress in nanophotonic biosensing. *Light.: Sci. Appl.* **13**, 76, https://doi.org/10.1038/s41377-024-01415-3 (2024).
24. Tselikov, G. I. et al. Topological Darkness: How to Design a Metamaterial for Optical Biosensing with Ultrahigh Sensitivity. *ACS Nano* **17**, 19338–19348, https://doi.org/10.1021/acsnano.3c06655 (2023).
25. Gaudin, M., Carles, P., Laborde, E., Champeaux, C. & Dumas-Bouchiat, F. A dual nanosecond-pulsed laser setup for nanocomposite synthesis—Ag nanoparticles in Al2O3/VO2 matrix. *J. Appl. Phys.* **125**, https://doi.org/10.1063/1.5058107 (2019).
26. Orlianges, J. -C. et al. Electrical and optical properties of vanadium dioxide containing gold nanoparticles deposited by pulsed laser deposition. *Appl. Phys. Lett.* **101**, https://doi.org/10.1063/1.4754708 (2012).
27. Niklasson, G. A., Granqvist, C. G. & Hunderi, O. Effective medium models for the optical properties of inhomogeneous materials. *Appl. Opt.* **20**, 26–30, https://doi.org/10.1364/AO.20.000026 (1981).
28. Flores, A., Robles, L., Arias, M. & Ascencio, J. Small metal nanoparticle recognition using digital image analysis and high resolution electron microscopy. *Micron* **34**, 109–118 (2003).
29. Ng, D. K., Bhola, B. S., Bakker, R. M. & Ho, S. T. Ultrasmooth gold films via pulsed laser deposition. *Adv. Funct. Mater.* **21**, 2587–2592 (2011).
30. Goos, F. & Hänchen, H. Ein neuer und fundamentaler Versuch zur Totalreflexion. *Ann. Phys.* **436**, 333–346, https://doi.org/10.1002/andp.19474360704 (1947).
31. Olaya, C. M., Hayazawa, N., Hermosa, N. & Tanaka, T. Angular Goos-Hanchen Shift Sensor Using a Gold Film Enhanced by Surface Plasmon Resonance. *J. Phys. Chem. A* **125**, 451–458, https://doi.org/10.1021/acs.jpca.0c09373 (2021).
32. Schwefel, H. G. L., Köhler, W., Lu, Z. H., Fan, J. & Wang, L. J. Direct experimental observation of the single reflection optical Goos-Hänchen shif. *Opt. Lett.* **33**, 794–796 (2008).
33. Kang, J. H. et al. Goos-Hanchen Shift and Even-Odd Peak Oscillations in Edge-Reflections of Surface Polaritons in Atomically Thin Crystals. *Nano Lett.* **17**, 1768–1774, https://doi.org/10.1021/acs.nanolett.6b05077 (2017).
34. Zhu, S. et al. Label-free biosensing with singular-phase-enhanced lateral position shift based on atomically thin plasmonic nanomaterials. *Light Sci. Appl* **13**, 2. https://doi.org/10.1038/s41377-023-01345-6 (2024).
35. Wu, F. et al. Giant enhancement of the Goos-Hänchen shift assisted by quasibound states in the continuum. *Phys. Rev. Appl.* **12**, 014028 (2019).
36. Zhou, X., Liu, S., Ding, Y., Min, L. & Luo, Z. Precise control of positive and negative Goos-Hänchen shifts in graphene. *Carbon* **149**, 604–608 (2019).
37. Wu, S., Ho, H., Law, W. C., Lin, C. & Kong, S. Highly sensitive differential phase-sensitive surface plasmon resonance biosensor based on the Mach–Zehnder configuration. *Opt. Lett.* **29**, 2378–2380 (2004).
38. Kamperman, T. et al. Spatiotemporal material functionalization via competitive supramolecular complexation of avidin and biotin analogs. *Nat. Commun.* **10**, 4347 (2019).
39. Opdahl, A., Petrovykh, D. Y., Kimura-Suda, H., Tarlov, M. J. & Whitman, L. J. Independent control of grafting density and conformation of single-stranded DNA brushes. *Proc. Natl. Acad. Sci.* **104**, 9–14, https://doi.org/10.1073/pnas.0608568103 (2007).
40. Herne, T. M. & Tarlov, M. J. Characterization of DNA Probes Immobilized on Gold Surfaces. *J. Am. Chem. Soc.* **119**, 8916–8920, https://doi.org/10.1021/ja9719586 (1997).
41. Loredo-García, E. et al. TNF-α Detection Using Gold Nanoparticles as A Surface-Enhanced Raman Spectroscopy Substrate. *Nanomedicine* **16**, 51–61, https://doi.org/10.2217/nnm-2020-0307 (2021).
42. Kukreja, L. M., Verma, S., Pathrose, D. A. & Rao, B. T. Pulsed laser deposition of plasmonic-metal nanostructures. *J. Phys. D: Appl. Phys.* **47**, 034015, https://doi.org/10.1088/0022-3727/47/3/034015 (2014).
43. Smalley, R. Laser studies of metal cluster beams. *Laser Chem.* **2**, 167–184 (1983).
44. Milani, P. & deHeer, W. A. Improved pulsed laser vaporization source for production of intense beams of neutral and ionized clusters. *Review of Scientific Instruments;(USA)* **61** (1990).
45. Perez, A. et al. Cluster assembled materials: a novel class of nanostructured solids with original structures and properties. *J. Phys. D: Appl. Phys.* **30**, 709 (1997).
46. Haberland, H., Insepov, Z. & Moseler, M. Molecular-dynamics simulation of thin-film growth by energetic cluster impact. *Phys. Rev. B* **51**, 11061 (1995).